# Water-gas shift reaction over platinum/strontium apatite catalysts

Dengyun Miao [a,b], Gülperi Cavusoglu [c,d], Henning Lichtenberg [c,d], Jiafeng Yu [a], Hengyong Xu [a], Jan-Dierk Grunwaldt [c,d], Andreas Goldbach [a,*]

[a] Dalian National Laboratory for Clean Energy, Dalian Institute of Chemical Physics, Chinese Academy of Sciences, 457 Zhongshan Road, 116023 Dalian, China
[b] University of Chinese Academy of Sciences, Beijing 100049, China
[c] Institute of Catalysis Research and Technology, Karlsruhe Institute of Technology, D-76344 Eggenstein-Leopoldshafen, Germany
[d] Institute for Chemical Technology and Polymer Chemistry, Karlsruhe Institute of Technology, D-76128 Karlsruhe, Germany

## ARTICLE INFO

## ABSTRACT

Platinum supported on calcium hydroxy (CaHAP) and fluoroapatite (CaFAP) exhibits excellent water-gas shift (WGS) activity comparable to the best Pt WGS catalysts on reducible oxides. The high activity of these unusual WGS catalysts is attributed to the parallel activation of CO on the noble metal and $H_2O$ on the ionic phosphates with formate species apparently being the major reaction intermediates. We have studied Pt supported on strontium hydroxy and fluoroapatites with varying cation and noble metal contents now in order to elucidate the role of the apatite cations and anions on WGS activity. Initial Pt dispersions approached 100% for loadings up to 3% (weight) with mean particle sizes of 1–2 nm according to $H_2$ chemisorption and EXAFS results (coordination number of 6.6). TEM analyses show further that the Pt aggregates grew slightly during catalytic testing up to 723 K with 1.5–2.5 nm particles being most abundant afterwards. Moreover, $Pt^{n+}$ reduction is much facilitated on these apatites as revealed by temperature programmed reduction coupled with *in situ* X-ray absorption spectroscopy (XAS). The WGS reaction rates in a reformate-type gas mixture increased strongly with Sr/P ratio in the apatite, with the rates over the most active Pt/SrHAP and Pt/SrFAP catalysts being among the highest reported to date. In particular, Pt/SrHAP and Pt/SrFAP rates surpassed the rates over analogous $Ca^{2+}$ substituted catalysts by ca. 30% at 573 K. This demonstrates that apatite cations have a strong impact on WGS conversion over these systems opening a route to catalysts with potentially even higher WGS activity.

© 2016 Elsevier B.V. All rights reserved.

## 1. Introduction

The water-gas shift (WGS) reaction $(CO + H_2O \leftrightarrows CO_2 + H_2, \Delta H = -41.1 \, kJ \, mol^{-1})$ is a very attractive option for CO clean up in decentralized production of high-purity $H_2$ for fuel cells because it does not consume $H_2$ but delivers additional fuel instead. In particular, its combination with micro and membrane reactor technology [1,2] is intriguing as compact devices can be obtained enabling on site $H_2$ production for transportation and residential proton exchange membrane fuel cell (PEMFC) applications [3,4]. However, conventional ferrochrome and Cu based catalysts are unsuitable for such systems due to their large weight and volume, long start-up times, insufficient durability under steady state and transient conditions, and high susceptibility to condensation and

poisoning [5,6]. High-temperature WGS reactors with integrated Pd membranes are also an intriguing option for pre-combustion $CO_2$ capture in large-scale power generation from fossil fuels [7–9]. This carbon capture scheme will benefit greatly from more active WGS catalysts because costly Pd membrane area can be reduced [2]. Hence, WGS catalysis has moved back to the forefront of research [5,6,10–18]. Gold and especially platinum supported on reducible oxides are the most promising alternatives for these WGS applications [5,6,10–14] although noble metal and rare earth element costs are a major concern [14]. These catalysts may also not be sufficiently stable under typical reformer outlet conditions [19,20].

Intrigued by an earlier study on the WGS reaction over apatite supported Au and Ru catalysts [21], we recently found that Pt supported on calcium hydroxyapatite $(Ca_{10}(PO_4)_6(OH)_2, CaHAP)$ exhibits excellent high-temperature WGS activity on par with the best ceria supported Pt catalysts reported in the literature and without showing propensity for methanation [22]. The variation of WGS activity with $Ca^{2+}$ surface concentration suggested that the apatite

cations play a crucial role in the WGS catalysis on these irreducible, ionic oxides. This hypothesis is supported by quantum chemical calculations which showed that $H_2O$ is strongly activated on apatite surfaces via simultaneous coordination to Lewis acidic $Ca^{2+}$ ions and H-bonding to basic O atoms of $PO_4^{3-}$ units [23,24]. Such simulations also revealed that formate ions are readily stabilized through similar bonding on CaHAP surfaces [25]. Interestingly, this species and its protonation product formic acid were the only WGS reaction intermediates that we detected by infrared (IR) spectroscopy on Pt/CaHAP catalysts [22].

Ionic apatites combine amphoteric acid and base functions and high hydrophilicity with good high-temperature stability [26–31]. These properties as well as the $Ca^{2+}$ concentration can be readily modified through formation of non-stoichiometric formulations $Ca_{10-Z}(HPO_4)_Z(PO_4)_{6-Z}(OH)_{2-Z}$ with $0 \leq Z \leq 1$ (i.e. $1.5 \leq Ca/P \leq 1.67$) and isomorphous cation and anion substitution [32]. Non-stoichiometric forms can be conveniently obtained by shifting the equilibrium between phosphate ions $PO_4^{3-}$ and its hydrogenated forms $HPO_4^{2-}$ and $H_2PO_4^-$ through variation of the pH value during precipitation of these materials from aqueous mixtures with concomitant adjustment of the number of charge balancing earth alkaline cations [31]. The Ca/P ratio can be even raised above the stoichiometric limit (1.67) with excess $Ca^{2+}$ ions being charge balanced by anions such as carbonate $CO_3^{2-}$ [26]. Since the WGS activity of Pt/CaHAP catalysts correlated strongly with $Ca^{2+}$ surface concentration [22], we have studied Pt supported on $Sr^{2+}$ exchanged hydroxyapatites and fluoroapatites now in order to further elucidate the impact of the support cations on the WGS activity of these materials. In addition to the $Sr^{2+}$ surface concentration we varied the Pt loading and carried out *in situ* XAS measurements to gain a better understanding of the interplay between the precious metal and apatites in WGS catalysis.

## 2. Experimental section

### 2.1. Catalyst preparation

All chemicals were of analytical grade, used without further purification and procured from Kermel unless otherwise noted. Strontium apatite powders were synthesized in analogous manner to previously studied Ca apatites [22] using aqueous solutions of $Sr(NO_3)_2$ and $(NH_4)_2HPO_4$ as precursors and aqueous ammonia (25%) for adjustment of the solutions pH values at 10, 10.5 and 11, respectively. Typically 100 mL aqueous 0.20 mol $L^{-1}$ $(NH_4)_2HPO_4$ solution (e.g. at pH 11) was added dropwise under vigorous magnetic stirring to 100 mL aqueous 0.33 mol $L^{-1}$ $Sr(NO_3)_2$ solution (e.g. at pH 11) at room temperature. The resulting suspension was kept stirring in a water bath for 2 h at 363 K and then cooled to room temperature and aged for 6 h. Next the precipitate was centrifuged, washed repeatedly with purified water until pH ~7, dried at 333 K for 12 h and finally calcined for 4 h in air at 773 K in a muffle furnace. The obtained powders were denoted SrHAP-10, SrHAP-10.5 and SrHAP-11 according to pH of the synthesis solutions. Fluoride substituted apatite (denoted SrFAP) was prepared by adding 0.247 g $NH_4F$ to the $(NH_4)_2HPO_4$ solution before combination with the $Sr(NO_3)_2$ solution (both at pH 11). The remaining procedural steps were the same as for preparation of the SrHAP powders.

Catalysts with nominally 1% Pt were prepared by impregnation of the calcined apatite powders at room temperature using appropriate amounts of aqueous 15.8 mg $mL^{-1}$ $H_2PtCl_6$ (Sinopharm Chemical Reagent Co.) solutions. The resulting suspensions were kept at room temperature for about 24 h before the samples were dried at 333 K for 12 h and calcined again for 4 h in air at 773 K in a muffle furnace. Pt/SrHAP-11 samples with different nominal Pt amounts (0.2–3%) were also prepared using the same method.

All Pt concentrations are based on catalyst weight unless otherwise noted and nominal Pt loading is prepended to catalyst designations where required for clarity (e.g. 1% Pt/SrHAP-11).

### 2.2. Catalyst characterization

The bulk Sr/P ratio and Pt content were analyzed with an inductively coupled plasma optical emission spectrometer (ICP-OES, Perkin-Elmer Optima 7300DV). For that purpose catalyst samples were digested with aqua regia in a hydrothermal reactor at 423 K for 2 h. Surface compositions of the as-prepared catalysts were determined by X-ray photoelectron spectroscopy (XPS) carried out with a Thermo ESCALAB 250Xi instrument using Al $K_\alpha$ radiation ($h\nu$ = 1486.6 eV). The C1s peak was set at 284.8 eV and taken as reference for binding energy calibration. The software XPSPEAK was used for fitting of XPS spectra employing a Shirley background and a 90/10 mixture of Gaussian and Lorentzian functions. Platinum dispersions were derived from $H_2$ chemisorption measurements at 323 K assuming that the molar ratio of adsorbed $H_2$ to exposed Pt is 0.5. Each catalyst (50 mg) was first reduced in flowing 10% $H_2$/Ar at 573 K for 1 h, heated to 698 K under Ar and kept at that temperature for 1 h to purge $H_2$, and then cooled to 323 K in Ar. Chemisorption measurements were performed at that temperature by injecting a series of 10% $H_2$/Ar pulses till saturation adsorption was reached.

The specific surface area was analyzed by the BET method carrying out $N_2$ adsorption measurements at 77 K on a QuadraSorb SI instrument (Quantachrome). All samples were used as powders and degassed at 573 K for 6 h in vacuum before $N_2$ adsorption. X-ray diffraction (XRD) patterns of the catalyst powders were recorded with a PANalytic Empyrean instrument using Cu $K_\alpha$ radiation ($\lambda$ = 0.1541 nm). Transmission electron microscopy (TEM) images were obtained with a JEM-2100 system (JEOL) with an acceleration voltage of 200 kV. The samples were ultrasonically suspended in ethanol and dropped onto a carbon film supported over a Cu grid for that purpose. Fourier transform infrared (FTIR) spectra were recorded in the 400–4000 $cm^{-1}$ range at a resolution of 4 $cm^{-1}$ on a Bruker Tensor 27 spectrometer equipped with a deuterated triglycinesulfate (DTGS) detector. Carefully ground catalyst samples were diluted with KBr (mass ratio = 1:200) and pressed into thin wafers for those measurements.

X-ray absorption near edge structure (XANES) and extended X-ray absorption fine structure (EXAFS) spectra of the 3% Pt/SrHAP-11 sample were recorded at ANKA-XAS at Angströmquelle Karlsruhe (ANKA, KIT, Germany) [33]. Measurements were performed at the Pt $L_3$-edge (11564 eV) in fluorescence mode using a Si(111) double crystal monochromator. A Pt foil was used for energy calibration. The intensity of the Pt $L_\alpha$-fluorescence (9.4 keV) was measured with an energy-dispersive 5-element solid-state Ge detector (Canberra, selected region: 9.1-9.7 keV, line width 300 eV). During temperature programmed reduction (TPR), XANES spectra were recorded in a continuous scanning mode (QEXAFS mode, scan duration 120 s). For this purpose, the 100–200 μm sieve fraction of the catalyst powder was loaded in a quartz capillary (outer diameter = 1.5 mm, wall thickness = 0.02 mm) between two quartz wool plugs. A gas blower (FMB Oxford) placed below the capillary was used for heating the sample from room temperature to 673 K at 5 K $min^{-1}$ while flowing a 5% $H_2$/He mixture (50 ml $min^{-1}$) through the capillary [34]. Before and after reduction EXAFS spectra were acquired in step scanning mode under steady state conditions at room temperature in flowing helium (50 ml $min^{-1}$). XANES and EXAFS data analysis was conducted using the Athena and Artemis interfaces of the IFEFFIT software package (version 0.8.056) [35]. The spectra were energy calibrated, normalized and background subtracted using Athena. Athena was also used for linear combination (LC) fitting of the XANES spectra to determine the relative concentrations of oxidized and reduced Pt species during TPR. LC analysis of XANES

**Table 1**
Textural characteristics of Pt/Sr apatite catalysts.

| Sample | $S_{BET}$[a] | $a$[b] | $c$[b] | $a/c$ | Pt[c] | D[d] | $d_{Pt}$[e] | Sr/P ratio | |
|---|---|---|---|---|---|---|---|---|---|
| | $(m^2 g^{-1})$ | (Å) | (Å) | | (wt.%) | (%) | (nm) | ICP[c] | XPS[f] |
| 1% Pt/SrHAP-10 | 16 | 9.794 | 7.297 | 1.342 | 0.74 | 83 | 1.4 | 1.72 | 1.74 |
| 1% Pt/SrHAP-10.5 | 30 | 9.806 | 7.286 | 1.346 | 0.83 | 94 | 1.2 | 1.74 | 1.86 |
| 0.2% Pt/SrHAP-11 | 26 | –[g] | – | – | 0.14 | – | – | – | – |
| 0.5% Pt/SrHAP-11 | 26 | – | – | – | 0.40 | 122 | 0.9 | – | – |
| 1% Pt/SrHAP-11 | 26 | 9.801 | 7.284 | 1.346 | 0.81 | 92 | 1.2 | 1.77 | 1.92 |
| 2% Pt/SrHAP-11 | 26 | – | – | – | 1.77 | 108 | 1.0 | – | – |
| 3% Pt/SrHAP-11 | 26 | 9.875 | 7.233 | 1.365 | 2.66 | 101 | 1.1 | – | 1.97 |
| 1% Pt/SrFAP | 54 | 9.733 | 7.299 | 1.333 | 0.87 | 100 | 1.1 | 1.84 | 2.05 |

[a] Support surface area (without Pt).
[b] Lattice parameter.
[c] ICP-OES analysis.
[d] Pt dispersion on as-prepared catalyst from $H_2$ chemisorption; note that the support was considered inert and a Pt/H ratio of 1:1 was assumed for the calculations.
[e] Pt particle diameter from $H_2$ chemisorption.
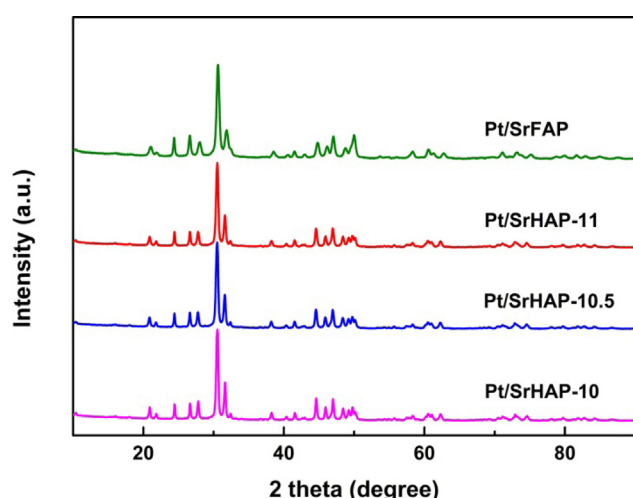[f] Calculated from Sr $3p_{3/2}$ and P $2s$ signals.
[g] Not analyzed.



**Fig. 1.** X-ray diffraction patterns of Pt/Sr-apatite samples with 1% nominal Pt loading.



**Fig. 2.** FTIR spectra of Pt/SrHAP and Pt/SrFAP samples with 1% nominal Pt loading. Note that the high wavenumber section on the left has been tenfold enlarged.

spectra was performed in the energy range from 20 eV below to 50 eV above the Pt $L_3$ edge using the first spectrum (denoted "oxidized") and the final spectrum (denoted "reduced", at 673 K) of the TPR series (XANES recorded in QEXAFS mode) as reference spectra.

### 2.3. Catalytic testing

WGS activity tests were carried out in a fixed-bed quartz tube reactor with a diameter of 8 mm at atmospheric pressure and temperatures between 523 K and 723 K. The calcined catalysts were ground to powder, pressed into a pellet at 20 MPa, crushed and sieved. The 40–60 mesh fraction (250–380 μm particles) of the as-prepared, calcined catalysts was used without prior reduction for determination of the light-off curves in a product-free reaction mixture (5% CO, 20% $H_2O$ in He). Typically 75 mg catalyst was diluted with 100 mg quartz sand of the same particle size range (40–60 mesh) and loaded into the quartz reactor. The height of the catalyst bed was about 5 mm. The reactor was heated under He to 523 K before the reactants were introduced. Water was injected into a preheater with a calibrated double-plunger pump (Elite P230) where it was vaporized and mixed with the dry feed gas components. Those measurements were carried out at GHSV = 150,000 mL $g_{cat}^{-1} h^{-1}$.

The 100–160 mesh fraction (96–150 μm particle size) of the catalysts was diluted with quartz sand particles in the same size range (100–160 mesh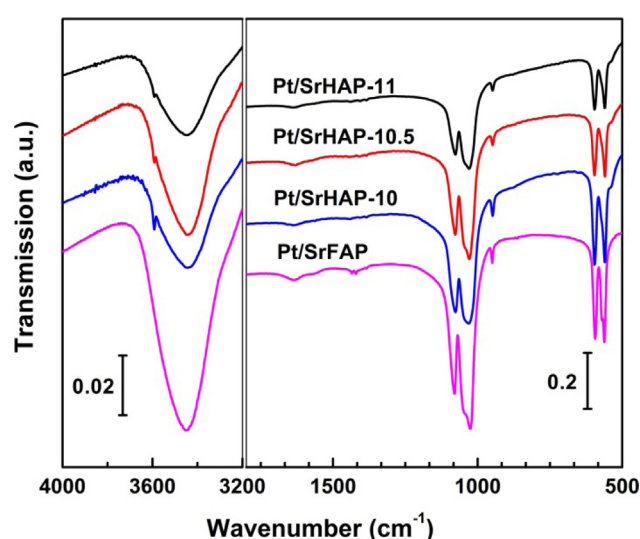) and used for measurement of reaction rates in a reformate-type gas mixture (15% CO, 5% $CO_2$, 30% $H_2O$, 40% $H_2$, 10% $N_2$). This feed mixture was adapted from modeling studies on $CO_2$ capture with WGS membrane reactors in natural gas combined cycle (NGCC) power plants [36]. The amount of catalyst was varied (20–200 mg) to limit CO conversion to 20% at maximum and the height of the catalyst bed was about 8 mm in these measurements. Samples were subjected to ca. 12 h conditioning in the reducing, product-free feed mixture at 673 K before these kinetic measurements because most of the WGS activity decline occurred within the initial 12 h during a stability test with a Pt/SrHAP sample (*vide infra*) in agreement with previous observations for a Pt/CaHAP catalyst [22].

The reactor tail gas was passed through a cooling trap where excess steam was condensed before feeding it to a gas chromatograph (Shimadzu GC-8A) equipped with a TDX-01 carbon molecular sieve column and a TCD for CO, $CO_2$, hydrocarbon and $H_2$ analysis. Only CO, $CO_2$ and $H_2$ were detected in the reactor exit stream but the latter could not be quantitatively analyzed because the GC was operated with He as carrier gas. Neither $CH_4$ nor any other side products were detected during any of the catalytic measurements indicating that their concentration was below the detection limit (<0.1%) in case they formed. Therefore, WGS
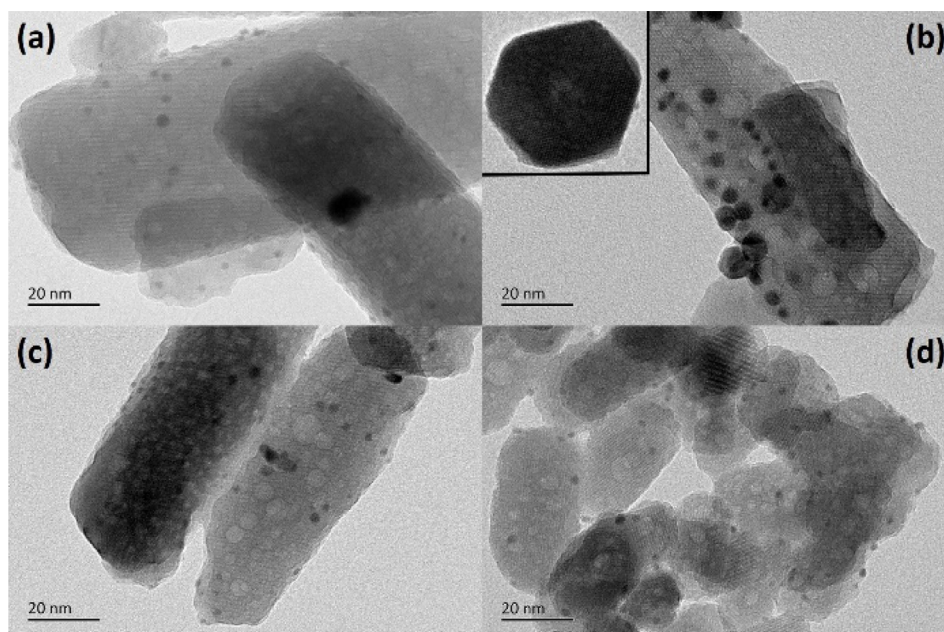
**Fig. 3.** TEM images of (a) Pt/SrHAP-10, (b) Pt/SrHAP-10.5, (c) Pt/SrHAP-11 and (d) Pt/SrFAP with 1% nominal Pt loading after catalytic testing.

conversion was identical with conversion of CO ($X_{CO}$) which was calculated according to

$$X_{CO} = \frac{[CO]_{in} - [CO]_{out}}{[CO]_{in}} \qquad (1)$$

where $[CO]_{in}$ and $[CO]_{out}$ are the CO concentrations in feed and tail gas, respectively. Thermodynamic equilibrium WGS CO conversions $X_{CO,eq}$ were calculated in analogous manner by replacing $[CO]_{out}$ in Eq. (1) with WGS equilibrium concentrations $[CO]_{eq}$ computed with the program *Gaseq* (http://www.arcl02.dsl.pipex.com/).

## 3. Results and discussion

### 3.1. Structural catalyst properties

Table 1 summarizes physical properties of the prepared catalysts with characterization focusing on the samples with 1% Pt loading. All diffraction patterns of the 1% Pt/SrHAP and 1% Pt/SrFAP catalysts (Fig. 1) are consistent with apatite patterns in the diffraction reference data base (SrHAP, JCPDS 00-033-1348: $a = 9.766$ Å, $c = 7.276$ Å, $a/c = 1.342$; SrFAP, JCPDS 00-050-1744: $a = 9.717$ Å, $c = 7.285$ Å, $a/c = 1.334$). The lattice parameters $a$ and $c$ of the apatite materials (Table 1) were derived from the (300) and (002) reflections, respectively, and matched well with those of the reference patterns. No diffraction peaks resulting from Pt or its oxides were observed for any Pt/Sr apatite sample not even at 3% nominal Pt loading insinuating that the particle size of Pt species remained below the XRD detection limit (ca. 4 nm). Fig. 2 shows the FTIR spectra of the 1% Pt/SrHAP and 1% Pt/SrFAP catalysts which are in good agreement with reported Sr apatite IR spectra [37]. The main difference between the fluoro and hydroxyapatite spectra is the missing $OH^-$ stretching band at 3591 cm$^{-1}$ in the Pt/SrFAP spectrum. This indicates that the hydroxide ions of the apatite structure can be completely substituted by fluoride ions as reported previously [22,27]. The bending and stretching vibrational modes of the $PO_4^{3-}$ ions at 561, 593, 949, 1026 and 1084 cm$^{-1}$ were slightly shifted to lower wave numbers in comparison to our CaHAP materials [22] and in agreement with previous observations [38]. The broad bands at 1632 and 3448 cm$^{-1}$ were due to absorbed water.

The specific surface area $S_{BET}$ ranged between 16 and 30 m$^2$ g$^{-1}$ for the hydroxyapatites but reached 54 m$^2$ g$^{-1}$ for the fluoroapatite (Table 1). Especially the surface areas of the SrHAP materials were significantly lower than those of the corresponding Ca$^{2+}$ exchanged apatites ($S_{BET} = 71–85$ m$^2$ g$^{-1}$) that we studied before [22]. However, they are in line with values reported previously for strontium hydroxyapatites [28,29]. Chemical analyses showed that the Sr/P molar ratio of the Sr-apatite materials increased with increasing synthesis pH value as it is the case for Ca apatites [22,31]. Surface Sr/P ratios resulting from XPS analyses (Table 1) were mostly larger than the bulk values, again in agreement with the literature [29]. The noble metal content of all Pt/apatite catalysts was somewhat lower than the targeted amount albeit very similar for the catalysts with nominally 1% Pt according to ICP-OES analyses. The Pt dispersions following from H$_2$ chemisorption were close to 100% on the as-prepared catalysts (Table 1). Dispersion values larger than 100% are most certainly a reflection of the errors associated with chemisorption and ICP-OES analyses which are bound to increase with decreasing Pt content.

Fig. 3 displays TEM images of the catalysts with 1% Pt after catalytic measurements in the product-free feed. The apatites formed large, rod shaped crystallites with hexagonal symmetry (inset Fig. 3b). The SrFAP crystallites were clearly smaller than the SrHAP ones which can explain the much higher surface area of the fluoroapatite catalyst. The noble metal particles were well dispersed although smaller Pt aggregates are difficult to discern on the massive apatite crystallites. Fig. 4 shows the corresponding Pt particle size distributions for which 200 particles were analyzed each at minimum. These distributions are very similar with 1.5–2.5 nm particles clearly being most abundant on all four catalysts. Apparently the Pt aggregates had slightly grown during catalytic testing between 523 K and 723 K. This is consistent with our previous findings for a 1% Pt/CaHAP catalyst where the mean Pt particle size had increased to ca. 2 nm after 100 h testing in the reformate-type mixture at 673 K.

Fig. 5 shows the Pt 4f XPS spectra of the as-prepared Pt/Sr apatite catalysts with 1% and 3% nominal Pt loading. The 1% Pt/SrHAP-11 spectrum can be well fitted using three doublet peaks which are assigned to the Pt$^0$, Pt$^{2+}$ and Pt$^{4+}$ oxidation states. Table 2 summarizes the Pt 4f$_{7/2}$ binding energies and relative concentrations
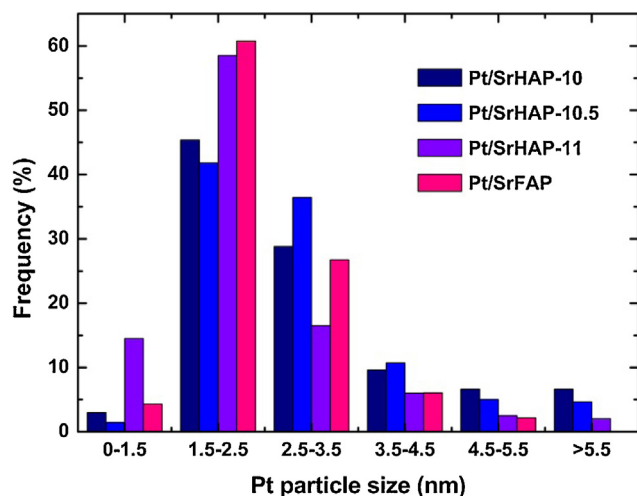
**Fig. 4.** Pt particle size distribution on Pt/SrHAP and Pt/SrFAP catalysts with 1% nominal Pt loading after catalytic testing in 5:20:75 CO/H₂O/He mixture.



**Fig. 6.** Pt L₃ XANES spectra of the 3% Pt/SrHAP-11 catalyst recorded during temperature programmed reduction.
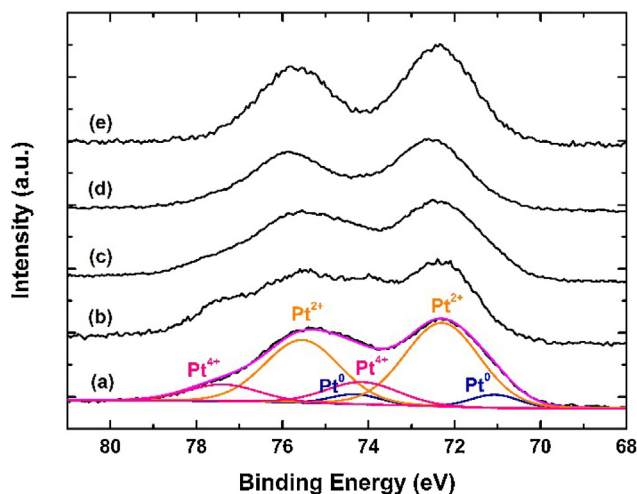


**Fig. 5.** Pt 4f XPS spectra of as-prepared catalysts: (a) 1% Pt/SrHAP-11, (b) 3% Pt/SrHAP-11, (c) 1% Pt/SrHAP-10.5, (d) 1% Pt/SrHAP-10 and (e) 1% Pt/SrFAP. The colored lines show the fitted $Pt^0$, $Pt^{2+}$, and $Pt^{4+}$ transitions for 1% Pt/SrHAP-11 as an example.



**Fig. 7.** Concentration of oxidized $Pt^{n+}$ species on 3% Pt/SrHAP-11 and 1% Pt/CeO₂ during temperature programmed reduction. The dashed lines follow from the derivative of the fitted solid lines and reflect H₂ consumption during TPR.

**Table 2**
Pt $4f_{7/2}$ binding energies and relative concentrations of Pt species on as-prepared Pt/Sr apatite catalysts.

| Catalyst | $Pt^0$ | | $Pt^{2+}$ | | $Pt^{4+}$ | |
|---|---|---|---|---|---|---|
| | eV | % | eV | % | eV | % |
| 3% Pt/SrHAP-11 | 71.1 | 0 | 72.3 | 69 | 74.1 | 31 |
| 1% Pt/SrHAP-11 | 71.1 | 8 | 72.3 | 73 | 74.2 | 19 |
| 1% Pt/SrHAP-10.5 | 71.2 | 6 | 72.4 | 73 | 74.3 | 21 |
| 1% Pt/SrHAP-10 | 71.0 | 3 | 72.5 | 81 | 74.1 | 16 |
| 1% Pt/SrFAP | 70.9 | 0 | 72.4 | 96 | 74.2 | 4 |

derived from such fitting of the five catalysts. The binding energies agree very well with reported values for $Pt^0$ (70.9 eV), $Pt^{2+}$ (72.4 eV) and $Pt^{4+}$ (74.2 eV) species supported on SrHAP [30]. It can be seen that $Pt^{2+}$ species were predominant on the hydroxyapatite catalysts with ca. 15–30% $Pt^{4+}$ and less than 10% $Pt^0$ species in addition. Interestingly, metal-like Pt appeared to be completely absent on the 3% Pt/SrHAP-11 and 1% Pt/SrFAP catalyst. On the other hand, only traces of the highest Pt oxidation state were found on the fluoroapatite catalyst while the $Pt^{4+}$ state was most abundant on the as-prepared catalyst with the highest noble metal loading. Note
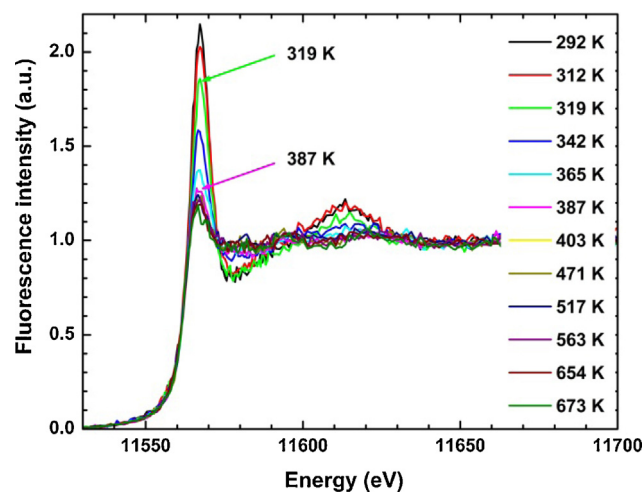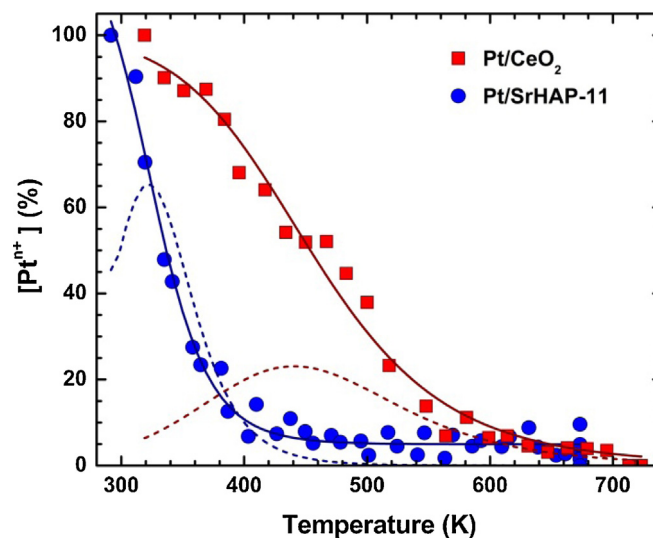
that the Sr 3p, P 2 s and O 1s XPS spectra were rather similar for all samples.

Fig. 6 shows selected Pt L₃ XANES spectra which were recorded *in situ* during heating of the 3% Pt/SrHAP-11 catalyst in a 5% H₂/He flow. The intensity of the white line (first strong resonance in the spectra) strongly depends on the Pt oxidization state: It will be high if oxidized Pt species ($Pt^{n+}$) dominate but rather weak if the majority of Pt atoms are in a metallic state ($Pt^0$) [39–41]. The low white line intensity at 387 K indicates that Pt has been largely reduced at this temperature. This is also evident from the LC fitting results presented in Fig. 7 revealing the relative concentrations of oxidized and reduced platinum species during TPR. For comparison we plotted also the corresponding reduction behavior of a highly active 1% Pt/CeO₂ WGS catalyst (*vide infra*) in this figure which was studied previously [42]. Obviously reduction of $Pt^{n+}$ species is much facilitated on the apatite in comparison with such species on the reducible CeO₂. Note that the dashed lines reflect H₂ consumption during TPR of the $Pt^{n+}$ species peaking around 325 K for 3% Pt/SrHAP-11 and around 440 K for 1% Pt/CeO₂.

Fig. 8 displays the XANES spectra of the 3% Pt/SrHAP-11 catalyst measured at room temperature before and after the TPR exper-

**Table 3**
Bond distances $R$, coordination numbers $CN$, and Debye-Waller Factors $\sigma^2$ for Pt-O and Pt-Pt bonds in 3% Pt/SrHAP-11 (the amplitude reduction factor $S_0^2$ was fixed at 0.84) and reference materials.

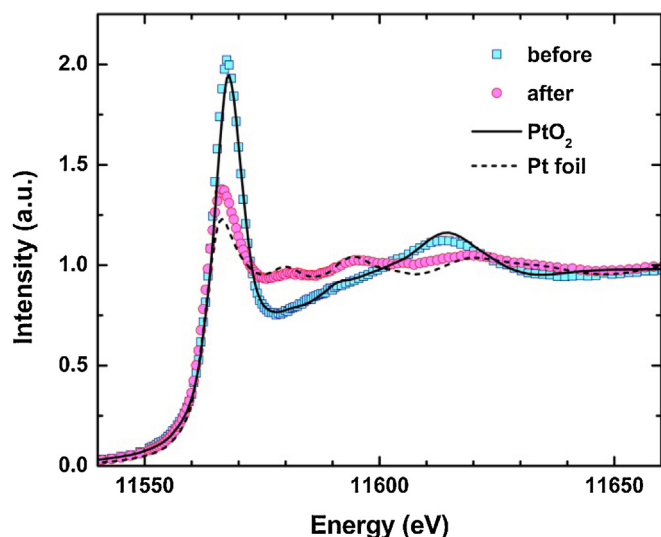| Sample | Interaction | $R$ [Å] | $CN$ | $\sigma^2 \times 10^{-2}$ [Å$^2$] | Comments |
|---|---|---|---|---|---|
| Pt/SrHAP-11 | Pt-O | 2.02 ± 0.04 | 4.7 ± 0.9 | 0.2 ± 0.2 | before TPR |
| Pt/SrHAP-11 | Pt-O | 2.02 ± 0.04 | – | 2 ± 0.7 | after TPR |
| | Pt-Pt | 2.76 ± 0.01 | 6.6 ± 2.1 | 0.5 ± 0.2 | |
| Pt foil | Pt-Pt | 2.76 | 12 | 0.5 ± 0.01 | Ref. [42] |
| PtO$_2$ | Pt-O | 2.02 | 6 | 0.2 ± 0.1 | Ref. [42] |
| PtO | Pt-O | 2.002 | 4 | 0.2 | Ref. [43] |
| PtO (XRD) | Pt-O | 2.019 | | | Ref. [44] |



**Fig. 8.** Pt L$_3$ XANES spectra of Pt foil, PtO$_2$ powder and 3% Pt/Sr/HAP-11 catalyst before and after reduction (recorded at room temperature).



**Fig. 9.** (a) Average k$^3$-weighted EXAFS and (b) corresponding Fourier-transformed EXAFS data of 3% Pt/SrHAP-11 recorded at room temperature before (top) and after (bottom) the TPR experiment. Solid lines indicate experimental data and dashed lines resulted from analytical data fitting. The data recorded before the TPR experiment has been offset for clarity of display.

iment as well as reference spectra of PtO$_2$ and a Pt foil measured previously at the same beamline [42]. The white line of the reduced Pt/Sr apatite sample was still more intense than that of the Pt foil which may indicate that a small fraction of oxidized Pt had survived the TPR treatment. This could be due to a strong interaction between the Pt aggregates and the ionic support material with Pt bonding to oxygen atoms of phosphate anions. Such residual ionic interactions should be conducive to the stabilization of very small Pt aggregates on apatite surfaces. On the other hand, the white line intensity is very sensitive to the Pt cluster geometry if the particles become very small [40]. In particular, the white line of cuboctahedral clusters (approximately spherical) should be practically identical with that of bulk Pt [39]. However, its intensity may grow significantly if Pt clusters adopt a more flat geometry [40] which is likely on supported catalysts as studied here. Fig. 8 further shows a rather good agreement between the XANES spectra of PtO$_2$ and the Pt/Sr apatite before reduction. Note that PtO$_2$ is routinely used as reference material for EXAFS analyses of oxidic Pt species on catalysts because PtO is difficult to prepare as bulk material.

Fig. 9 presents the average k$^3$-weighted EXAFS data and corresponding Fourier-transformed data of the 3% Pt/SrHAP-11 catalyst measured at room temperature before and after the TPR experiment along with analytical fitting curves. Table 3 compiles bond lengths $R$, coordination numbers $CN$ and Debye-Waller factors $\sigma^2$ derived from fitting of those data. For comparison also corresponding parameters are included for PtO$_2$ and a Pt foil obtained earlier at the same beamline [42] as well as for PtO from reported EXAFS [43] and crystal structure [44] analyses. The Fourier-transformed data of the Pt/Sr apatite shows a single peak before reduction (Fig. 9b, top) for which the fitting yields a bond distance of 2.02 Å and coordination number of 4.7. Table 3 shows that this value is consistent
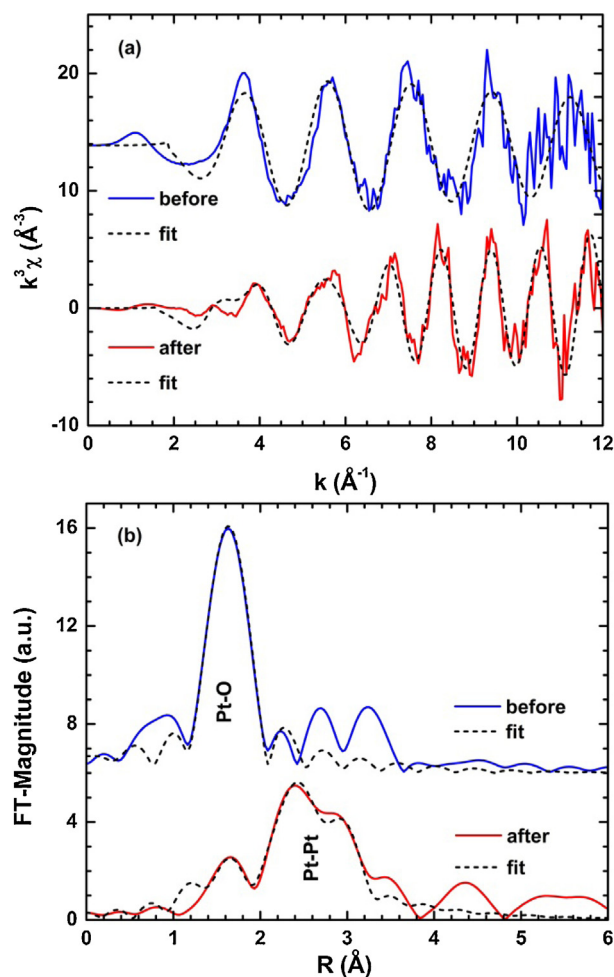
with the Pt-O bond distances in PtO$_2$ and PtO. The corresponding Fourier transform also has a weak peak at this Pt-O distance after reduction of the Pt/Sr apatite but it is dominated by an interaction at longer distance (Fig. 9b, bottom). Fitting yields a bond distance of 2.76 Å for this latter interaction which matches very well with the Pt-Pt distance derived for the Pt foil (Table 3). The Pt-Pt coordination number of 6.6 is much smaller than for bulk Pt. This low value is consistent with ca. 1 nm wide, flat Pt aggregates according to a reported relationship [45] and thus in good agreement with the values derived from H$_2$ chemisorption for the as-prepared sample (Table 1). The fit yields also a Pt–O bond distance of 2.02 Å after the TPR experiment but the corresponding coordination number is small confirming the Pt species had been mostly reduced following

**Table 4**
WGS reaction rates and activation energies of Pt catalysts at 573 K.

| Catalyst | Pt wt.% | $r_{cat}$ $\mu mol_{CO}$ $g_{cat}^{-1}$ $s^{-1}$ | $r_{Pt}$ $mol_{CO}$ $mol_{Pt}^{-1}$ $s^{-1}$ | $E_{act}$ kJ $mol^{-1}$ | notes |
|---|---|---|---|---|---|
| 1% Pt/SrHAP-10 | 0.74 | 1.7 | 0.05 | 72 | this work |
| 1% Pt/SrHAP-10.5 | 0.83 | 18.3 | 0.43 | 71 | this work |
| 1% Pt/SrHAP-11 | 0.81 | 29.3 | 0.70 | 70 | this work |
| 1% Pt/SrFAP | 0.87 | 36.0 | 0.81 | 70 | this work |
| Pt/CaHAP-10.5 | 0.77 | 21.6[a] | 0.55 | 83 | Ref. [22] |
| Pt/CaFAP | 0.78 | 24.0[a] | 0.60 | 81 | Ref. [22] |
| Pt/CeO$_2$ | 0.74 | 16.0[a] | 0.42 | 82 | Ref. [22] |
| Pt/CeO$_2$/Al$_2$O$_3$ | 0.9 | 27[b] | 0.59 | 70 | Ref. [46] |
| Pt-4Na-TiO$_2$ | 1 | 58.6[c] | 1.14 | 80 | Ref. [47] |
| Pt/P25-34Na | 1 | 35.9[d] | 0.70 | 77 | Ref. [48] |
| Pt/Ca$_{0.5}$Ce$_{0.5}$O$_{1.5}$ | 0.5 | 12.5[e] | 0.49 | | Ref. [14] |
| Pt/Ce(La)O$_x$ NaCN leached | 3.06[f] | 73.7[g] | 0.47 | 75 | Ref. [49] |

[a] Reactant composition: 15% CO, 30% H$_2$O, 5% CO$_2$, 40% H$_2$, 10% N$_2$.
[b] Reactant composition: 10% CO, 20% H$_2$O, 10% CO$_2$, 30% H$_2$, 30% Ar.
[c] Reactant composition: 2.83% CO, 5.66% H$_2$O, 37.74% H$_2$, 53.77% He.
[d] Reactant composition: 6.8% CO, 21.9% H$_2$O, 8.5% CO$_2$, 37.4% H$_2$, 25.4% Ar.
[e] Reactant composition: 3.0% CO, 26.1% H$_2$O, 29.9% H$_2$, 3.7% N$_2$, 37.3% He; Pt dispersion was estimated at 75% assuming 1.5 nm hemispherical particles according to an established method [42,50].
[f] Pt content calculated from bulk atomic Pt/Ce/La ratio assuming CeO$_2$ and La$_2$O$_3$.
[g] Reactant composition: 11% CO, 26% H$_2$O, 7% CO$_2$, 26% H$_2$, 30% He.
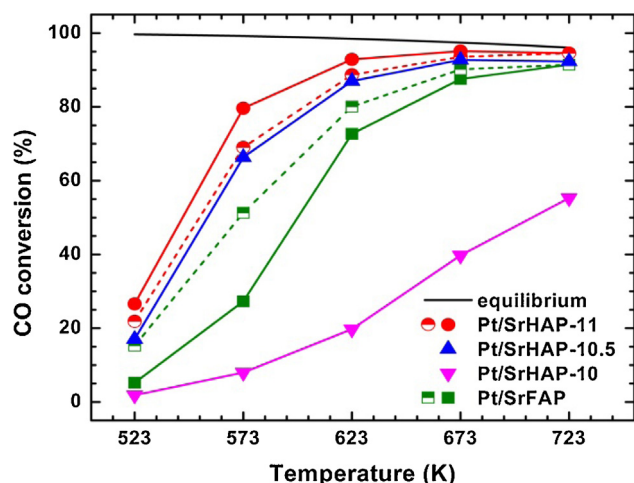


**Fig. 10.** Water-gas shift light-off curves for Pt/SrHAP and Pt/SrFAP catalysts with 1% nominal Pt loading in a 5:20:75 CO/H$_2$O/He mixture. Solid symbols and lines show CO conversion during initial temperature increase and half-filled symbols with dashed lines show CO conversion during subsequent temperature decrease.



**Fig. 11.** Stability of 1% Pt/SrHAP-11 catalyst in reformate-type feed gas at 573 K.

the TPR experiment. This enduring Pt—O bonding may also reflect the abovementioned stabilizing interactions between Pt clusters and the ionic apatite.

### 3.2. Catalytic reaction

Fig. 10 shows CO conversion over the 1% Pt/SrHAP and 1% Pt/SrFAP catalysts as function of temperature in the product-free reaction mixture. The general trends are similar to those found previously for Pt supported on CaHAP and CaFAP catalysts. Methane formation was not observed and carbon dioxide was the only carbonaceous product. The WGS activity of the Pt/SrHAP catalysts increased with surface Sr/P ratio (Table 1) with $X_{CO}$ approaching equilibrium conversion over Pt/SrHAP-11 and Pt/SrHAP-10.5 at 673 K while remaining far away from equilibrium even at 723 K over the least WGS active Pt/SrHAP-10 catalyst. The initial CO conversion was also lower over the Pt/SrFAP catalyst than over Pt/SrHAP-10.5 and Pt/SrHAP-11. However, WGS activity of Pt/SrFAP had improved noticeably after testing at higher temperatures while that of the Pt/SrHAP-11 catalyst had been slightly reduced. The Pt/SrHAP-11 catalyst also showed minor deactivation during operation in the reformate-type mixture at 573 K (Fig. 11) with CO
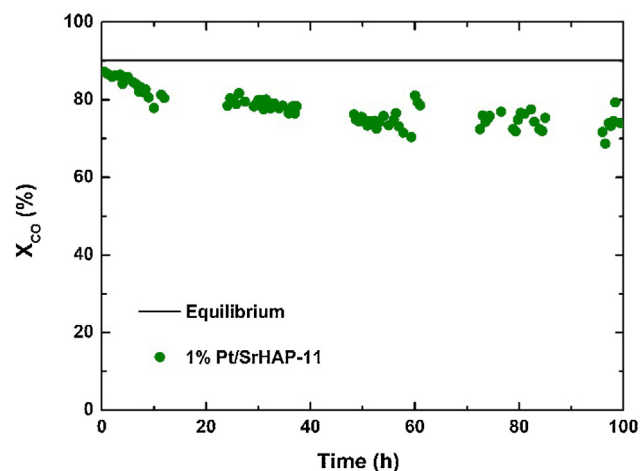
conversion declining mostly within the first 12 h. Therefore we conditioned the catalysts in the product-free feed overnight at 673 K before measurement of reaction rates.

Carbon monoxide conversions were limited to less than 20% during measurements in the reformate mixture in order to determine reaction rates $r_{cat}$ based on total catalyst weight between 573 K and 673 K. Activation energies $E_{act}$ were derived from Arrhenius plots of those reaction rates as shown in Fig. 12. The resultant WGS kinetic quantities are compared in Table 4 with published values of Pt catalysts [14,22,46–49] that had been obtained in reformate mixtures as well. For ease of comparison between catalysts with differing Pt content, we tabulated reaction rates $r_{Pt}$ normalized to Pt amount, too. These normalized reaction rates confirm a strong correlation of WGS activity with Sr/P ratio on the apatite surface, i.e. Pt/SrFAP (Sr/P = 2.05) > Pt/SrHAP-11 (Sr/P = 1.92) > Pt/SrHAP-10.5 (Sr/P = 1.86) ≫ Pt/SrHAP-10 (Sr/P = 1.74). Table 4 shows that $r_{Pt}$ reaction rates of the best Pt/Sr apatite catalysts were ca. 30% higher than those obtained previously for Pt/Ca apatite catalysts at 573 K under the same experimental conditions. This is remarkable as especially $S_{BET}$ of Pt/SrHAP catalysts was more than 50% smaller than that of their counterparts supported on calcium hydroxyapatites ($S_{BET} \geq 70$ m$^{-2}$ g$^{-1}$) [22].

On the other hand, apatite surface area does appear to impact the reaction rates at higher Pt concentrations as can be seen from
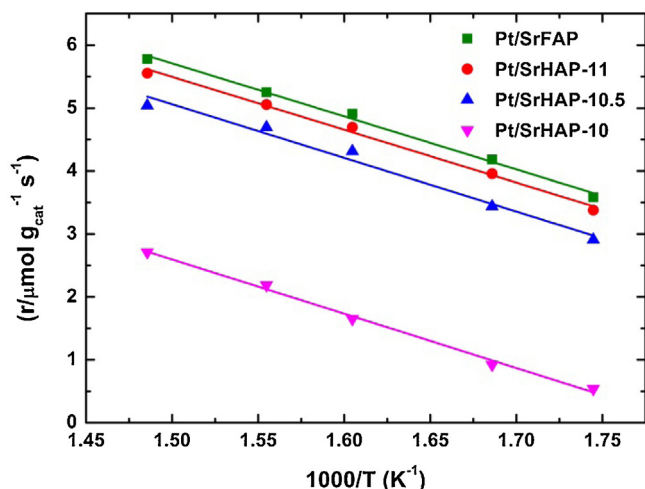
**Fig. 12.** WGS rates over Pt/SrHAP and Pt/SrFAP catalysts with 1% nominal Pt loading in reformate-type feed gas at 573–673 K.



**Fig. 13.** WGS rates over Pt/SrHAP-11 catalysts with different Pt loading in reformate-type feed gas at 573 K and 673 K. Note that rates at 573 K were multiplied by a factor 10.

the Pt normalized rates $r_{Pt}$. Fig. 13 shows $r_{cat}$ as function of Pt loading on SrHAP-11 at 573 K and 673 K. Note that the $r_{cat}$ reaction rates were approximately 10 times higher at 673 K than at 573 K. They increased linearly with Pt amount up to 1% with the slope of the line corresponding to $r_{Pt} = 0.68\ mol_{CO}\ mol_{Pt}^{-1}\ s^{-1}$ at 573 K, in good agreement with the tabulated $r_{Pt}$ value of the 1% Pt/SrHAP-11 catalyst. This indicates that the Pt normalized reaction rate was constant for Pt loadings up to 1%. However, $r_{cat}$ grew only weakly when the Pt concentration was further raised so that $r_{Pt}$ came down to 0.24 $mol_{CO}\ mol_{Pt}^{-1}\ s^{-1}$ at 573 K for the largest Pt loading. This drop off does not appear to be due to Pt particle size variations as those were rather similar in the investigated Pt concentration range according to the chemisorption analyses (Table 1). Therefore, we suppose that the Pt particle density exceeded the optimum value on the Sr apatite surface at noble metal contents above 1%.

The WGS mechanism on noble metal catalysts is still strongly disputed together with the associated reaction intermediates [6,10,51–54]. Formate-like adducts have been often postulated as main WGS reaction intermediates [10,51,52] while others consider them as spectator species [53,54]. Alternatively, carboxyl-like adducts have been proposed as key WGS reaction intermediates supported by computational simulations [53,55] but no spectroscopic evidence has been presented for them to date [56]. In fact, there may be several reaction pathways operational on WGS catalysts with relative contributions depending on reaction conditions [6,57]. For example, formate decomposition into $CO_2$ and $H_2$ was slow under low-temperature WGS conditions but accelerated when steam was co-adsorbed [51,58]. Nevertheless, without bias towards mechanistic details, we note that we detected only formate and its protonation product formic acid as potential reaction intermediates during *in situ* IR measurements on Pt/CaHAP catalysts [22].

We have attributed the excellent WGS activity of these systems to the facile activation of $H_2O$ and subsequent stabilization of reaction intermediates on apatite surfaces [22]. The activation of $H_2O$ is considered to be more challenging than that of CO in the water-gas shift reaction [5]. For example, both experimental and computational investigations have shown that dissociation of $H_2O$ is the rate-determining step in low-temperature WGS catalysis on Cu surfaces [53,59] and water activation was also attributed a key role in structured Pt/CeO$_2$/Al$_2$O$_3$ WGS catalysts [60]. It has been long known too that doping with alkali metals promotes significantly the WGS reaction over supported Pt catalysts [61]. Addition of Ca has a similar effect on WGS conversion rates over Pt/CeO$_2$
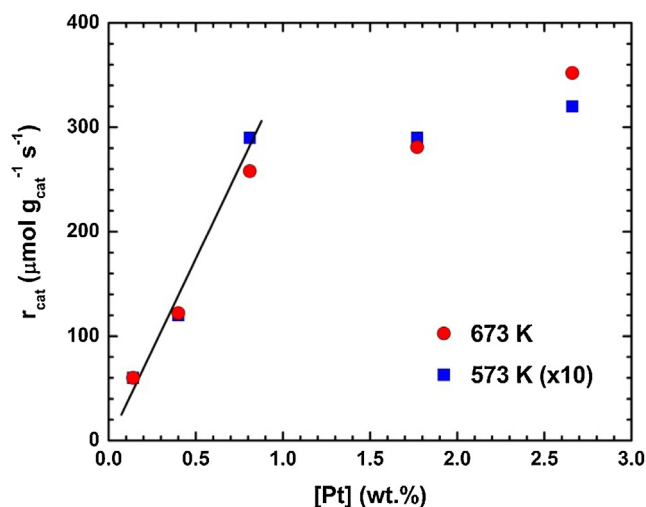
and Pt/TiO$_2$ catalysts [14,62,63]. The promotional effect of Ca on the WGS conversion is still under debate. It was postulated that oxygen vacancies are created at the platinum-support interface as a result of Ca addition where both CO and $H_2O$ may be adsorbed and activated [62,63]. Alternatively, the mobility of O-bound reaction intermediates could be improved facilitating the decomposition of e.g. reaction intermediates such as formate into $CO_2$ and $H_2$ [14].

It is not clear whether these effects are operative in the systems studied here but computational simulations [23–25] have shown that the apatite $Ca^{2+}$ cations play a crucial role in $H_2O$ activation and formate stabilization on apatite surfaces. Water molecules adsorb in a strongly polarized fashion on apatite surfaces through simultaneous coordination to Lewis acidic $Ca^{2+}$ and – *via* H bonding – basic O atoms of $PO_4^{3-}$ ions, favoring dissociation and rendering them highly reactive [23,24]. Such modeling further revealed that bonding of formate ions on apatite surfaces also involves two to three $Ca^{2+}$ ions and H bonding to $OH^-$ ions resultant from $H_2O$ dissociation [25]. Thus, it seems likely that CO and $H_2O$ form similar, transient adducts involving coordination to Pt and several apatite surface ions during WGS conversion on the systems studied here. Simultaneous bonding of reaction intermediates to multiple surface cations can account in a straightforward manner for the pronounced increase of WGS activity with surface cation concentration. Therefore, the remarkable WGS activity of Pt/apatite catalysts appears to be strongly associated with the apatite cations. This conclusion is corroborated by the $r_{Pt}$ rates which are noticeably higher over the Pt/SrHAP-11 and Pt/SrFAP catalysts than over their best $Ca^{2+}$ substituted counterparts (Table 4). Evidently, the substitution of $Ca^{2+}$ with $Sr^{2+}$ appears to enhance the WGS reaction rates over Pt supported on apatite materials markedly.

On the other hand, WGS activity may also benefit from the enhanced reducibility of the catalytic Pt species on apatites. Thus, considering the much more difficult reduction of $Pt^{n+}$ species on CeO$_2$ revealed by the *in situ* XAS-TPR experiments (Fig. 7), it is not surprising that the $r_{Pt}$ rates over the apatite based catalysts surpassed those reported for high performance Pt WGS catalysts supported on ceria (Table 4) at 573 K. This includes the aforementioned highly active Pt/CeO$_2$ catalyst prepared in our laboratory [22]. To date, Na promoted Pt/TiO$_2$ catalysts yielded the highest $r_{Pt}$ rates among Pt WGS catalysts supported on reducible oxides at 573 K [47,48] to the best of our knowledge. The reaction rates are noticeably higher over these catalysts in $CO_2$ free mixtures [47] while they come down to the range of the Pt/Sr apatite catalysts

with $CO_2$ present due to $CO_2$ inhibition [48]. The turnover frequency (TOF) reached values around 3.8 over these alkali promoted Pt/TiO$_2$ catalysts exceeding those over our Pt/SrHAP-11 (TOF = 0.77 s$^{-1}$) and Pt/SrFAP (TOF = 0.81 s$^{-1}$) catalysts by a factor of 5 almost. However, this is foremost a reflection of the relatively low Pt dispersion on these Na promoted Pt/TiO$_2$ catalysts (28%) [48]. Obviously, the Pt normalized reaction rates $r_{Pt}$ are more interesting from a practical perspective as they reflect the effective utilization of the precious metal. Hence, the remarkable WGS activity of Pt/apatite catalysts can be also attributed in part to apatites being conducive to high Pt dispersion and stabilization of very small Pt clusters.

## 4. Conclusion

Noble metal dispersion was close to 100% on Pt/Sr hydroxy and fluoroapatite catalysts with up to 3% nominal Pt loading according to H$_2$ chemisorption results. This corresponds to a mean Pt particle size around 1.1 nm which is supported by the low average Pt-Pt coordination number of 6.6 derived from EXAFS data. The mean aggregate size grew only slightly during WGS testing up to 723 K according to TEM measurements. The WGS activity increased strongly with Sr/P ratio on the support surface without exhibiting any methanation activity up to 723 K. The $r_{cat}$ reaction rates on a Pt/SrHAP catalyst increased linearly with Pt content up to ca. 1% but only moderately above that concentration possibly due to apatite surface area limitations. The Pt normalized reaction rates over the best of these systems rank among the highest reported for Pt WGS catalysts at 573 K so far. In particular, the rates determined here exceeded those observed previously for Pt/Ca apatite catalysts under the same experimental conditions by 30%. This corroborates that apatite cations play a crucial role in WGS conversion over these catalysts. Temperature programmed reduction with simultaneous *in situ* XAS measurements further revealed that oxidized Pt species can be much more easily reduced on apatites than on reducible oxides like CeO$_2$. This enhanced reducibility of Pt species is likely to contribute to the exceptional WGS activity of Pt/apatite catalysts, too. XAS results (enhanced Pt L$_3$ white line intensity, Pt-O contribution in the EXAFS data) point to some residual ionic character of Pt species after reduction at 673 K. This could indicate interactions between the ionic support and Pt clusters that stabilize rather small Pt clusters on apatites. These features and the very high catalytic activity of Pt/apatite catalysts render them an attractive option for high-temperature WGS microreactors and membrane reactors where severe spatial limitations exist for catalyst beds.

## References

[1] P. Piermartini, T. Schuhmann, P. Pfeifer, G. Schaub, Top. Catal. 54 (2011) 967–976.
[2] Y. Bi, H. Xu, W. Li, A. Goldbach, Int. J. Hydrogen Energy 34 (2009) 2965–2971.
[3] L. Cornaglia, J. Munera, E. Lombardo, Int. J. Hydrogen Energy 40 (2015) 3423–3437.
[4] A. Brunetti, G. Barbieri, E. Drioli, Fuel Process. Technol. 92 (2011) 166–174.
[5] K.G. Azzam, I.V. Babich, K. Seshan, L. Lefferts, J. Catal. 251 (2007) 153–162.
[6] C.M. Kalamaras, D.D. Dionysiou, A.M. Efstathiou, ACS Catal. 2 (2012) 2729–2742.
[7] K. Damen, M. van Troost, A. Faaij, W. Turkenburg, Prog. Energy Combust. Sci. 32 (2006) 215–246.
[8] A. Goldbach, F. Bao, C. Qi, C. Bao, L. Zhao, C. Hao, C. Jiang, H. Xu, Int. J. Greenhouse Gas Control 33 (2015) 69–76.
[9] L.C. Ma, B. Castro-Dominguez, N.K. Kazantzis, Y.H. Ma, Int. J. Greenhouse Gas Control 42 (2015) 424–438.
[10] E. Chenu, G. Jacobs, A.C. Crawford, R.A. Keogh, P.M. Patterson, D.E. Sparks, B.H. Davis, Appl. Catal. B: Environ. 59 (2005) 45–56.
[11] Q. Fu, W.L. Deng, H. Saltsburg, M. Flytzani-Stephanopoulos, Appl. Catal. B: Environ. 56 (2005) 57–68.
[12] X.S. Liu, W. Ruettinger, X.M. Xu, R. Farrauto, Appl. Catal. B: Environ. 56 (2005) 69–75.
[13] T.R. Reina, S. Ivanova, M.A. Centeno, J.A. Odriozola, Appl. Catal. B: Environ. 187 (2016) 98–107.
[14] L.Z. Linganiso, G. Jacobs, K.G. Azzam, U.M. Graham, B.H. Davis, D.C. Cronauer, A.J. Kropf, C.L. Marshall, Appl. Catal. A: Gen. 394 (2011) 105–116.
[15] T. Noor, M.V. Gil, D. Chen, Appl. Catal. B: Environ. 150 (2014) 585–595.
[16] M.N. Moreira, A.M. Ribeiro, A.F. Cunha, A.E. Rodrigues, M. Zabilskiy, P. Djinovic, A. Pintar, Appl. Catal. B: Environ. 189 (2016) 199–209.
[17] L.Z. Zhang, J.M.M. Millet, U.S. Ozkan, Appl. Catal. A: Gen. 357 (2009) 66–72.
[18] S.S. Maluf, P.A.P. Nascente, C.R.M. Afonso, E.M. Assaf, Appl. Catal. A: Gen. 413 (2012) 85–93.
[19] J.M. Zalc, V. Sokolovskii, D.G. Loffler, J. Catal. 206 (2002) 169–171.
[20] W. Ruettinger, X.S. Liu, R.J. Farrauto, Appl. Catal. B: Environ. 65 (2006) 135–141.
[21] A. Venugopal, M.S. Scurrell, Appl. Catal. A: Gen. 245 (2003) 137–147.
[22] D. Miao, A. Goldbach, H. Xu, ACS Catal. 6 (2016) 775–783.
[23] M. Corno, C. Busco, V. Bolis, S. Tosoni, P. Ugliengo, Langmuir 25 (2009) 2188–2198.
[24] V. Bolis, C. Busco, G. Martra, L. Bertinetti, Y. Sakhno, P. Ugliengo, F. Chiatti, M. Corno, N. Roveri, Philos. Trans. R. Soc. A 370 (2012) 1313–1336.
[25] P. Canepa, F. Chiatti, M. Corno, Y. Sakhno, G. Martra, P. Ugliengo, Phys. Chem. Chem. Phys. 13 (2011) 1099–1111.
[26] M.I. Dominguez, F. Romero-Sarria, M.A. Centeno, J.A. Odriozola, Appl. Catal. B: Environ. 87 (2009) 245–251.
[27] Y. Zhang, J. Wang, J. Yin, K. Zhao, C. Jin, Y. Huang, Z. Jiang, T. Zhang, J. Phys. Chem. C 114 (2010) 16443–16450.
[28] S. Ogo, A. Onda, K. Yanagisawa, Appl. Catal. A: Gen. 348 (2008) 129–134.
[29] S. Ogo, A. Onda, Y. Iwasa, K. Hara, A. Fukuoka, K. Yanagisawa, J. Catal. 296 (2012) 24–30.
[30] A. Ono, Y. Takahashi, S. Kato, M. Ogasawara, T. Wakabayashi, Y. Nakahara, S. Nakata, Res. Chem. Intermed. 37 (2011) 1225–1230.
[31] T. Tsuchida, J. Kubo, T. Yoshioka, S. Sakuma, T. Takeguchi, W. Ueda, J. Catal. 259 (2008) 183–189.
[32] N.J. Flora, K.W. Hamilton, R.W. Schaeffer, C.H. Yoder, Synth. React. Inorg. Met. Org. Chem. 34 (2004) 503–521.
[33] J.D. Grunwaldt, S. Hannemann, J. Goettlicher, S. Mangold, M.A. Denecke, A. Baiker, Phys. Scr. T. 115 (2005) 769–772.
[34] J.-D. Grunwaldt, N. van Vegten, A. Baiker, Chem. Commun. (2007) 4635–4637.
[35] B. Ravel, M. Newville, J. Synchr. Radiat. 12 (2005) 537–541.
[36] K. Atsonios, K.D. Panopoulos, A. Doukelis, A. Koumanakos, E. Kakaras, Energy Convers. Manage. 60 (2012) 196–203.
[37] Y. Gangarajula, R. Kedharnath, B. Gopal, Appl. Catal. A: Gen. 506 (2015) 100–108.
[38] J. Terra, E.R. Dourado, J.-G. Eon, D.E. Ellis, G. Gonzalez, A.M. Rossi, Phys. Chem. Chem. Phys. 11 (2009) 568–577.
[39] A.L. Ankudinov, J.J. Rehr, J.J. Low, S.R. Bare, Top. Catal. 18 (2002) 3–7.
[40] A.L. Ankudinov, J.J. Rehr, J.J. Low, S.R. Bare, J. Chem. Phys. 116 (2002) 1911–1919.
[41] M. Huebner, D. Koziej, M. Bauer, N. Barsan, K. Kvashnina, M.D. Rossell, U. Weimar, J.-D. Grunwaldt, Angew. Chem. Int. Ed. 50 (2011) 2841–2844.
[42] G. Cavusoglu, D. Miao, H. Lichtenberg, H.W.P. Carvalho, H. Xu, A. Goldbach, J.-D. Grunwaldt, Appl. Catal. A: Gen. 504 (2015) 381–390.
[43] N. Torapava, L.I. Elding, H. Maendar, K. Roosalu, I. Persson, Dalton Trans. 42 (2013) 7755–7760.
[44] J.R. McBride, G.W. Graham, C.R. Peters, W.H. Weber, J. Appl. Phys. 69 (1991) 1596–1604.
[45] A. Puig-Molina, F.M. Cano, T.V.W. Janssens, J. Phys. Chem. C 114 (2010) 15410–15416.
[46] O. Thinon, F. Diehl, P. Avenier, Y. Schuurman, Catal. Today 137 (2008) 29–35.
[47] X. Zhu, M. Shen, L.L. Lobban, R.G. Mallinson, J. Catal. 278 (2011) 123–132.
[48] J.H. Pazmino, M. Shekhar, W.D. Williams, M.C. Akatay, J.T. Miller, W.N. Delgass, F.H. Ribeiro, J. Catal. 286 (2012) 279–286.
[49] Q. Fu, H. Saltsburg, M. Flytzani-Stephanopoulos, Science 301 (2003) 935–938.
[50] G. Bergeret, in: P. Gallezot, G. Ertl, H. Knözinger, F. Schüth, J. Weitkamp (Eds.), Handbook of Heterogeneous Catalysis, vol. 1, Wiley-VCH, Weinheim, 2008, pp. 738–765.
[51] G. Jacobs, B.H. Davis, Int. J. Hydrogen Energy 35 (2010) 3522–3536.
[52] T. Shido, Y. Iwasawa, J. Catal. 141 (1993) 71–81.
[53] A.A. Gokhale, J.A. Dumesic, M. Mavrikakis, J. Am. Chem. Soc. 130 (2008) 1402–1414.
[54] D. Tibiletti, A. Goguet, F.C. Meunier, J.P. Breen, R. Burch, Chem. Commun. (2004) 1636–1637.
[55] X.Q. Gong, P. Hu, R. Raval, J. Chem. Phys. 119 (2003) 6324–6334.
[56] P. Gao, U.M. Graham, W.D. Shafer, L.Z. Linganiso, G. Jacobs, B.H. Davis, Catal. Today 272 (2016) 42–48.

[57] C.M. Kalamaras, I.D. Gonzalez, R.M. Navarro, J.L.G. Fierro, A.M. Efstathiou, J. Phys. Chem. C 115 (2011) 11595–11610.
[58] Y. Iwasawa, Accts. Chem. Res. 30 (1997) 103–109.
[59] C.T. Campbell, K.A. Daube, J. Catal. 104 (1987) 109–119.
[60] M. González-Castaño, S. Ivanova, O.H. Laguna, L.M. Martínez T, M.A. Centeno, J.A. Odriozola, Appl. Catal. B: Environ. 200 (2017) 420–427.
[61] Y. Amenomiya, G. Pleizier, J. Catal. 76 (1982) 345–353.
[62] P. Panagiotopoulou, J. Papavasiliou, G. Avgouropoulos, T. Ioannides, D.I. Kondarides, Chem. Eng. J. 134 (2007) 16–22.
[63] P. Panagiotopoulou, D.I. Kondarides, Appl. Catal. B: Environ. 101 (2011) 738–746.